Progress In Electromagnetics Research, Vol. 139, 539–558, 2013

CYLINDRICAL MICROSTRIP ARRAY ANTENNAS WITH SLOTTED STRIP-FRAMED PATCHES

Alexander Ye. Svezhentsev[1, *], Vladimir Kryzhanovskiy[1], and Guy A. E. Vandenbosch[2]

[1]Usikov Institute of Radiophysics and Electronics, National Academy of Sciences of the Ukraine, 12, Acad. Proskury str, Kharkov 61085, Ukraine

[2]Katholieke Universiteit Leuven, Div. ESAT-TELEMIC, Kasteelpark Arenberg 10, B-3001 Leuven, Belgium

Abstract—A cylindrical microstrip array antenna with 5 pairs of coupled slotted strip framed patches is analyzed. The patches are proximity-fed by a cylindrical microstrip line. In order to extract the reflection coefficient from the standing wave pattern on the microstrip line, its length is about 5 wavelengths. To the best of the authors' knowledge proximity-fed cylindrical arrays have not been analyzed before using a rigorous MOM model that takes into account all electromagnetic couplings between patches and feeding line. The paper consists of three parts. The first part describes a plane wave excitation of the cylindrical microstrip structure. It introduces some innovating theoretical developments, like the improvement of the asymptote for the spectral Green's function and the explicit surface wave contribution. The second part calculates the radar cross section of the cylindrical microstrip structure with single and coupled slotted strip framed patches. The resonant frequencies, and the amplitude and phase of the current distribution are analysed. The third part describes a design for a proximity-fed array of 5 coupled slotted strip framed patches. It gives the reflection coefficient, current distribution on the patches, and radiation pattern. A very low level of cross polarization ($< -40\,\mathrm{dB}$) is achieved. It is shown that the resonant frequencies of the cylindrical array and its planar analogue lie very close to each other. This is due to the common nature of the low frequency slot resonance for the slotted strip framed patch.

Received 19 March 2013, Accepted 3 May 2013, Scheduled 9 May 2013

* Corresponding author: Alexander Ye. Svezhentsev (alexan1999@yandex.ru).

1. INTRODUCTION

In recent years, cylindrical microstrip antennas (CMAs) have been intensively analysed by different methods [1–19]. Several characteristics of CMAs such as the radiation pattern [8–19], input impedance versus frequency [10–16, 17, 18], radar cross-section (RCS) [19], and far field versus frequency in particular directions (RCS analogue) [16] have been studied in the literature. The excitation of the CMA can be via a cylindrical microstrip line (CML) [7, 12, 13, 17], a probe [14, 16, 18], or a plane wave [19]. In most cases, the analysis has been performed with the method of moments (MoM) in both spectral [10, 12, 13, 15, 17–19] and spatial [7, 11, 14, 16, 18] domains. The usage of entire-domain basis functions (defined over the entire patch area) [10, 11, 15] for the analysis, limits the application of MoM to rectangular cylindrical structures. Arbitrarily shaped patches need sub-domain basis functions. They have been used for a rectangular cylindrical patch with recessed feed [7, 13], a U-shaped patch [17], an E-shaped patch [18], and rectangular cylindrical patches with variously shaped slots [19].

One of today's problems is designing cylindrical microstrip antenna arrays with shaped patches fed by a microstrip line. From planar antenna analysis [20–22] it is known that the patches can be fed using either direct electrical contact (strong coupling) with the microstrip line or using proximity coupling (weak coupling). To the best of the authors' knowledge cylindrical microstrip antenna arrays with shaped patches proximity-fed by a CML have not been rigorously analysed in the literature as yet.

This paper uses a proper patch shape in an effort to realize weak coupling between the array components and the feeding CML, simultaneously providing linear polarization of the radiation field (low-level cross polarization). Weak coupling means that the power on the CML should be coupled to the array elements not too quickly, in order to permit multi-element antenna arrays, and at the same time not too slowly, so that as much power as possible is indeed coupled to the global array.

The choice of the slotted strip-frame patch, which is shaped to the rectangular cylindrical form and is made of a strip with a slot, is based on the authors' experience with familiar complex-shape patches. This topology is expected to be very suitable in view of the specific features needed for the patch current amplitude and phase distributions: when the E-vector of the excitation field is parallel to the slotted side of the patch, the radiation field has predominantly a linear polarization. It is worth mentioning that, to the knowledge of the authors, no

slotted strip-frame patches of this kind have ever been used in printed planar or cylindrical antennas [23–37]. It is clearly shown in this paper that slotted strip-frame patches are effective for cylindrical microstrip antenna arrays (CMAAs) fed by a cylindrical microstrip line.

The theoretical analysis is carried out with the method of moments in the spectral domain [13, 17, 19], exploiting, as in [17, 19], piecewise sinusoidal (PWS) basis functions. The existing MoM scheme in [13, 17, 19] has been upgraded, namely, considering some more asymptotic terms in the spectral Green's function, which reduces simulation times. Also, the surface wave contribution to the mutual impedance matrix has been explicitly derived. The reflection coefficient in the feeding CML is considered as a function of frequency. The patch current distributions and the CMAA radiation patterns are examined at resonant frequencies. For comparison, a similar planar microstrip antenna array has been analyzed with the simulation package Sonnet 12.53.

2. CYLINDRICAL MICROSTRIP STRUCTURE WITH SLOTTED STRIP-FRAME PATCHES

2.1. Problem Formulation and Solution by the Moment Method in the Spectral Domain

The cylindrical microstrip structure (CMS) under analysis is shown in Fig. 1(a). It is based on the so-called Goubau line [38], and consists of a z-infinite circular metal cylinder of radius r_1 with a dielectric coated cylinder of radius r_0 and relative permittivity ε_r backing a slotted strip-frame metal patch. The single and coupled patch versions are

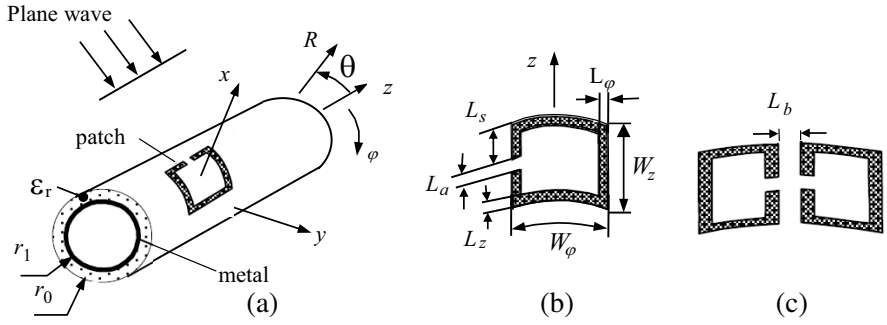

Figure 1. (a) CMS with a slotted strip-frame patch excited by a plane wave, (b) single slotted strip-frame patch, and (c) pair of coupled slotted strip-frame patches.

presented in Figs. 1(b) and 1(c).

The plane wave

$$\mathbf{E}^{inc} = \mathbf{E}^0 e^{jk_0 x} \tag{1}$$

with a unit amplitude ($|\mathbf{E}^0| = 1$) travels from infinity along the x-axis to be normally incident on the patch surface. In formulae (1) $k_0 = 2\pi/\lambda_0$, where λ_0 is the free space wavelength. The time dependence $e^{j\omega t}$ is assumed and suppressed throughout. In the cylindrical coordinate system (r, φ, z) the z-components of the electric and magnetic fields of the incident plane wave can be written as [39]

$$E_z^{inc}(r,\varphi) = \sum_{n=-\infty}^{n=\infty} a_{nz}(r) e^{-jn\varphi}, \tag{2}$$

$$H_z^{inc}(r,\varphi) = \sum_{n=-\infty}^{n=\infty} \bar{a}_{n\,z}(r) e^{-j\,n\varphi}, \tag{3}$$

with

$$a_{n\,z}(r) = W_0 \cos(\gamma) j^n J_n(k_0 r) \tag{4}$$

$$\bar{a}_{nz}(r) = \sin(\gamma) j^n J_n(k_0 r), \tag{5}$$

where W_0 is the free space wave impedance, $J_n(x)$ the Bessel function of the first kind of order n and argument x, and γ the polarization parameter. For $\gamma = 0°$, the E vector is parallel to the z-axis. For $\gamma = 90°$, the E vector is parallel to the y-axis.

It is required to find the patch current distribution produced by the incident field. For this purpose, using the equivalence theorem [40], the metal patch is substituted by the equivalent surface (sheet) electric current distributed on the patch surface, S'. The current density $\mathbf{J}_s^e(r_0, \varphi', z')$ on the surface S' is unknown, with the subscript s standing for z or φ. The total tangential electric field is represented by the sum of the excitation field caused by the incident field and the scattered field produced by the equivalent surface current in view of the two partial domains: $p = 0$ for $r \geq r_0$ and $p = 1$ for $r_0 > r > r_1$. Specifically,

$$E_s^p(r,\varphi,z) = E_s^{p,exc}(r,\varphi,z) + E_s^{scat,J}(r,\varphi,z), \tag{6}$$

where

$$\mathbf{E}_s^{scat,J}(r,z,\varphi) = \int_{z'} \int_{\varphi'} \hat{\mathbf{G}}^J(r,r_0,z,z',\varphi,\varphi') \cdot \begin{bmatrix} \mathbf{J}_z^e(r_0,\varphi',z') \\ \mathbf{J}_\varphi^e(r_0,\varphi',z') \end{bmatrix} dS', \tag{7}$$

with the Green function

$$\hat{\mathbf{G}}^J(r,r_0,z,z',\varphi,\varphi') = \begin{bmatrix} G_{zz}^J(r,r_0,z,z',\varphi,\varphi') & G_{z\varphi}^J(r,r_0,z,z',\varphi,\varphi') \\ G_{\varphi z}^J(r,r_0,z,z',\varphi,\varphi') & G_{\varphi\varphi}^J(r,r_0,z,z',\varphi,\varphi') \end{bmatrix} \tag{8}$$

The excitation field $E_s^{p,exc}(r, \varphi, z)$ is taken from the diffraction problem solution [19] for a plane wave given by (1) incident on the Goubau line. The derivation of (7) is available from [10]. The boundary condition that the total tangential electric field (6) vanishes on the substituted metal patch surface yields the following integral equation for the unknown surface current density

$$-\mathbf{E}_s^{0,exc}(r_0, z, \varphi) = \int_{z'}\int_{\varphi'} \hat{\mathbf{G}}^J(r_0, r_0, z, z', \varphi, \varphi') \cdot \begin{bmatrix} \mathbf{J}_z(r_0, \varphi', z') \\ \mathbf{J}_\varphi(r_0, \varphi', z') \end{bmatrix} dS'. \quad (9)$$

It should be borne in mind that the current and the Green's function components are evaluated at the interface $r = r_0$. Integral Equation (9) is solved by the method of moments using Galerkin's scheme. The unknown surface current density is expanded using the basis functions

$$\mathbf{J} = \mathbf{J}_z + \mathbf{J}_\varphi = \sum_{i=1}^{NB} \alpha_i \mathbf{J}_{s,i}^b, \quad (10)$$

where

$$\mathbf{J}_{s,i}^b (i = 1, \ldots, NB) = \begin{cases} \mathbf{J}_{z,i}^b & i = 1, \ldots, NBZ \\ \mathbf{J}_{\varphi,i}^b, & i = 1 + NBZ, \ldots, NBZ + NB\varphi \end{cases}. \quad (11)$$

Here α_i, $i = 1, \ldots, NB$ are the unknown coefficients and $NB = NBZ + NB\varphi$ is the total number of basis functions, where $NBZ = (NZ - 1) \times N\varphi$, $NB\varphi = (N\varphi - 1) \times NZ$, and NZ and $N\varphi$ are the number of z- and φ-subdivisions, respectively.

By the method of moments, integral Equation (9) is reduced to a system of linear algebraic equations (SLAE)

$$\mathbf{Z}\boldsymbol{\alpha} = \mathbf{V}, \quad (12)$$

where $\boldsymbol{\alpha}[i] = \alpha_i$. Matrix $\mathbf{Z}$ is a block matrix

$$\mathbf{Z} = \left[Z_{i,k}^{p,q}\right] = \begin{bmatrix} Z_{i1,k1}^{z,z} & Z_{i1,k2}^{z,\varphi} \\ Z_{i2,k1}^{\varphi,z} & Z_{i2,k2}^{\varphi,\varphi} \end{bmatrix}, \quad (13)$$

where $i1$, $k1 = 1, \ldots, NBZ$ and $i2$, $k2 = 1 + NBZ, \ldots, NBZ + NB\varphi$. The elements of matrix (13) evaluated in the spectral domain are

$$Z_{i,k}^{p,q} = \frac{1}{4\pi^2} \sum_{n=-\infty}^{\infty} \int_{-\infty}^{\infty} \tilde{\mathbf{J}}_{pi}^t(-n, -h)\, \hat{\tilde{\mathbf{G}}}^J(n, h)\, \tilde{\mathbf{J}}_{qk}^b(n, h) dh, \quad (14)$$

where $(p, q = z, \varphi)$, $k = 1, \ldots, NB$, and $\tilde{\mathbf{J}}_{pi}^t(-n, -h)$, $\tilde{\mathbf{J}}_{qk}^b(n, h)$, and $\hat{\tilde{\mathbf{G}}}^J(n, h)$ are the spectral equivalents of $\mathbf{J}_{pi}^t$, $\mathbf{J}_{q\,k}^b$, and $\hat{\mathbf{G}}^J$,

respectively. Function $\mathbf{J}_{pi}^{t}$ is the test function coinciding with the basis functions (11) (Galerkin's scheme). The ith element of the column $\mathbf{V} = \{V_i^s\,(i = 1, \ldots, NB\}$, where number i is as in (11), is evaluated in the spatial domain as follows

$$V_i^s = -\iint\limits_{S_i} ds' \mathbf{J}_{si}^{t} \mathbf{E}_s^{0,exc}(r_0, z, \phi), \quad (s = z, \varphi) \tag{15}$$

Here surface S_i is the domain of the ith test function. The spectral Green's function $\hat{\tilde{\mathbf{G}}}^{J}(r_{\mathbf{0}}, n, h)$ is available from [16]. The Fourier transforms of the basis functions and the final computational formula for the V_i^s elements are given in [19].

2.2. Effective Evaluation of the Mutual Impedance Matrix

A direct numerical evaluation of (14) presents a number of problems. First, a large computation time is required as the spectral Green's function components involve cylindrical functions. To speed up the calculations, we adopt the remedy applied during the evaluation of the input impedance of a CML-fed CMA (strong coupling) introduced in [12]. It consists of the separation of the asymptotic terms out of the spectral Green's function. For the first time, asymptotic representations of spectral Green's function components were heuristically obtained in [12] by combining the available plane-case formulas with the asymptotic cylindrical-case expressions for the two limiting relationships $h \gg n$ and $h \ll n$ between cylindrical function index n and propagation constant h. Now with the uniform asymptotes [41, 42] of the modified cylindrical functions, the asymptotes of the spectral Green's function components $\tilde{G}_{pq}^{J,AS}(h, n)$ can be directly evaluated in pure cylindrical terms with the formulas

$$\tilde{G}_{z\,z}^{J,AS}(h, n) = \frac{j\bar{h}^2}{\sqrt{n^2 + (k_0 r_0)^2 \bar{h}^2}} \frac{k_0 r_0}{(\varepsilon_r + 1)} \Delta(n, h, r_0 - r_1) \tag{16}$$

$$\tilde{G}_{z\,\varphi}^{J,AS}(h, n) = \frac{j\bar{h}n}{\sqrt{n^2 + (k_0 r_0)^2 \bar{h}^2}} \frac{1}{(\varepsilon_r + 1)} \Delta(n, h, r_0 - r_1) \tag{17}$$

$$\tilde{G}_{\varphi\,\varphi}^{J,AS}(h, n) = \frac{jn^2}{(k_0 r_0)\sqrt{n^2 + (k_0 r_0)^2 \bar{h}^2}} \frac{\Delta(n, h, r_0 - r_1)}{(\varepsilon_r + 1)}, \tag{18}$$

where $\bar{h} = h/k_0$,

$$\Delta(n, h, r_0 - r_1) = 1 - e^{-2\sqrt{(n)^2 + (k_0 r_0)^2 \bar{h}^2}(r_0 - r_1)/r_0}, \tag{19}$$

Formulas (16)–(18) differ from the corresponding expressions in [12] by an additional factor Δ in (19). Considering the Green's

function [42, 43] in the mixed potential form, one finds that the second term in the right-hand side of (19) represents the source image inside an infinite, dielectrically coated circular cylinder.

Another trouble with a direct evaluation of (14) is the singular behaviour of the spectral Green's function components at the poles associated with the Goubau line surface waves. Normally the pole is avoided by deforming the real-axis path of integration into the complex plane of the propagation constant. In our case, the path of integration always stays on the real axis, and the spectral function component behavior at the poles is compensated by the subtraction of the specially designed function [19] given by

$$\tilde{G}_{pq}^{J,SURF}(h,n) = \frac{2R_n^{(pq)m}P_n^m}{\bar{h}^2 - (P_n^m)^2} \tag{20}$$

with $\bar{h} = P_n^m$ ($n = 0, \ldots, N$ and $m = 1, \ldots, M_n$), where N is the largest azimuth index n at which the surface waves still exist, M_n the largest number of the surface waves for the azimuth index n fixed, and $R_n^{(pq)m}$ the residue of a the spectral Green's function component $\tilde{G}_{pq}^{J}(h,n)$ at a pole $\bar{h} = P_n^m$. Poles have been found and investigated in [42] using the Newton method. The residues $R_n^{(pq)m}$ can be calculated numerically.

With Green's function asymptotes (16)–(18) and function (20) to compensate the singular behavior at the surface wave poles, expression (14) becomes

$$Z_{ik}^{(p,q)} = Z_{ik}^{(p,q),CYL} + Z_{ik}^{(p,q),AS} + Z_{ik}^{(p,q),SURF}, \tag{21}$$

where

$$Z_{i,k}^{(p,q),CYL} = \frac{1}{4\pi^2}\sum_{n=-\infty}^{\infty}\int_{-\infty}^{\infty}\tilde{\mathbf{J}}_{pi}^{t}(-n,-h)\hat{\tilde{\mathbf{G}}}1^{J}(n,h)\tilde{\mathbf{J}}_{qk}^{b}(n,h)dh \tag{22}$$

$$Z_{i,k}^{(p,q),AS} = \frac{1}{4\pi^2}\sum_{n=-\infty}^{\infty}\int_{-\infty}^{\infty}\tilde{\mathbf{J}}_{pi}^{t}(-n,-h)\hat{\tilde{\mathbf{G}}}^{J,AS}(n,h)\tilde{\mathbf{J}}_{qk}^{b}(n,h)dh \tag{23}$$

$$Z_{i,k}^{(p,q),SURF} = \frac{1}{4\pi^2}\sum_{n=-\infty}^{\infty} I_{i,k}^{(p,q),SURF}(n) \tag{24}$$

$$\tilde{\hat{G}}1(n,h) = \tilde{\hat{G}}(n,h) - \tilde{\hat{G}}^{AS}(n,h) - \tilde{G}_{pq}^{J,SURF}(h,n) \tag{25}$$

$$I_{ik}^{(p,q),SURF}(n) = \int_{-\infty}^{\infty}\tilde{\mathbf{J}}_{pi}^{t}(-n,-h)\hat{\tilde{\mathbf{G}}}^{J,SURF}(n,h)\tilde{\mathbf{J}}_{qk}^{b}(n,h)dh \tag{26}$$

Through the Fourier transformants of the basis and the test functions presented in a form [19]

$$\tilde{\mathbf{J}}_{p,i}^{b(t)}(n,h) = \tilde{J}_{p,i}^{b(t)}(n,h)\mathbf{e}_p^0 = e^{jz_i^{b(t)}h} e^{jn\varphi_i^{b(t)}} a_p^n(n) a_p^h(h) \mathbf{e}_p^0, \tag{27}$$

where $\mathbf{e}_p^0$ is the unit vector in the z or φ direction. $a_p^n(n)$ and $a_p^h(h)$ are given in [19]. $z_i^{b(t)}$ and $\varphi_i^{b(t)}$ are the centers of basis (test) function location, respectively. Expression (26) is written as

$$I_{ik}^{(p,q),SURF}(n) = e^{-jn\left(\varphi_i^t - \varphi_k^{b)}\right)} a_p^n(-n) a_q^n(n) f^{(p,q)}(n) \tag{28}$$

where

$$f^{(p,q)}(n) = \int\limits_{-\infty}^{\infty} e^{-jh\left(z_i^t - z_k^b\right)} a_p^h(-h) \mathbf{e}_p^0 \hat{\tilde{\mathbf{G}}}^{J,SURF}(n,h) a_q^h(h) \mathbf{e}_q^0 dh \tag{29}$$

The evaluation of the integral (29) implies closing the integration contour in the upper or the lower half-plane (depending on the $z - z'$ sign) and employing the residue theorem as in [42]. The result is

$$f^{(p,q)}(n) = -2\pi i k_0 \sum_{m=1}^{M_n} R_n^m a_p^h\left(-P_n^m\right) a_q^h\left(P_n^m\right) e^{\pm i P_n^m k_0 \left(z_i^t - z_k^b\right)} \tag{30}$$

The sign $\pm$ is chosen depending on whether $z_i^t - z_k^b < 0(+)$ or $> 0(-)$.

2.3. Radar Cross Section Analysis

The solution of Equation (12) yields the patch current distribution and, hence, the field at any point of space, including the far field $\vec{E}^{scat,J}(R, \theta, \varphi)$. Then the RCS can be calculated as

$$\sigma_{u\nu} = \frac{4\pi R^2 \left|\vec{E}^{scat,J}(R, \theta = \pi/2, \varphi = 0) \cdot \vec{i}_\nu\right|^2}{\left|\vec{E}_u^0\right|^2} \tag{31}$$

Here $u, \nu = \theta, \varphi$, $|\vec{E}_u^0|$ is the field amplitude of the incident plane wave polarized in the u-direction, $\vec{i}_\nu$ the unit vector in the ν-direction, and $\vec{E}^{scat,J} \cdot \vec{i}_\nu$ the ν-field component in the direction $\theta = \pi/2$, $\varphi = 0$.

Assume that the analyzed CMS in Fig. 1 has $r_1 = 0.025\,\text{m}$, $\varepsilon_r = 2.2$, and $r_0/r_1 = 1.0316$. Fig. 2 presents the numerically calculated RCS, $\sigma_{\theta\theta}/\sigma_0$ (where $\sigma_0 = \pi W_z W_\varphi$ is the normalizing factor) versus frequency. Curve 1 is for the slotted strip-frame patch, curve 2 is for the pair of coupled strip-frame patches, and curve 3 is for the custom rectangular cylindrical patch,whose size is the same as in [13],

having dimensions $W_z = W_\varphi = 5.04\,\text{cm}$ in the z- and φ-directions, respectively. The resonant frequency of this patch is $f = 1.9825\,\text{GHz}$, see Fig. 2, which is very close to the value $f = 2.001\,\text{GHz}$ (the difference is about 1%) observed in [13]. Here we use the same mesh as in [13], namely, with 10 and 42 segments in the z- and φ-directions, respectively. The segment size is $L_z = 0.504\,\text{cm}$ and $L_\varphi = 0.12\,\text{cm}$ in the z- and φ-directions, respectively. To get the slotted strip-frame patch from the rectangular cylindrical patch in the frame of the same mesh we can remove some segments in such a way that the slotted strip-frame patch fits a size of 8×16 segments having $W_z = 4.032\,\text{cm}$, $W_\varphi = 1.92\,\text{cm}$ as overall dimensions (see Fig. 1(b)). The slot is located in a symmetrical way, namely $W_z = 2L_s + L_a$, where $L_s = 1.512\,\text{cm}$, $L_a = 1.008\,\text{cm}$. The patch profile of the pair of coupled slotted strip-frame patches was constructed in a similar way with the only difference that the original rectangular cylindrical patch is split in to 10×39 segments (39 segments instead of 42). Then the pair of coupled slotted strip-frame patches is formed from the rectangular cylindrical patch by removing some segments in such a way that eventually it fits a size of 8×19 segments in the z- and φ-directions, respectively, having $W_z = 4.032\,\text{cm}$, $W_\varphi = 1.032\,\text{cm}$, $L_\varphi = 0.129\,\text{cm}$, $L_s = 1.512\,\text{cm}$, $L_a = 1.008\,\text{cm}$, $L_z = 0.504\,\text{cm}$, and $L_b = 0.387\,\text{cm}$.

Notice that in the φ-direction, the single strip-frame patch is twice as long as each patch in the pair of coupled strip-frame patches. This is why the resonant frequency of the single patch is evidently lower than the resonant frequency of the pair of coupled strip-frame patches.

The amplitude and phase distributions of the z- and φ-components of the current density for the pair of coupled strip-frame patches are

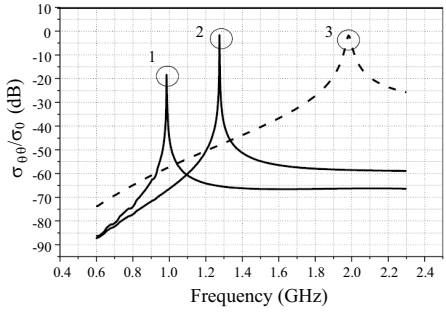

Figure 2. CMA radar cross section $\sigma_{\theta\theta}/\sigma_0$ and resonant frequencies f for different-shape patches: 1 — slotted strip-frame patch, $f_1 = 0.985\,\text{GHz}$, 2 — pair of coupled slotted strip-frame patches, $f_2 = 1.275\,\text{GHz}$, and 3 — rectangular cylindrical patch, $f_3 = 1.9825\,\text{GHz}$.

presented in Figs. 3 and 4. The z-component of the current is mainly concentrated on the slot-opposite conducting strips (W_z), with no phase shift between these currents.

For the single patch, the amplitude of the φ-component of the current is similarly distributed on both φ-directed conducting strips, with a 180° phase shift between them. For the pair of strip-frame patches, the amplitude and phase distributions of the current z-component are symmetric with respect to the plane $\varphi = 0°$.

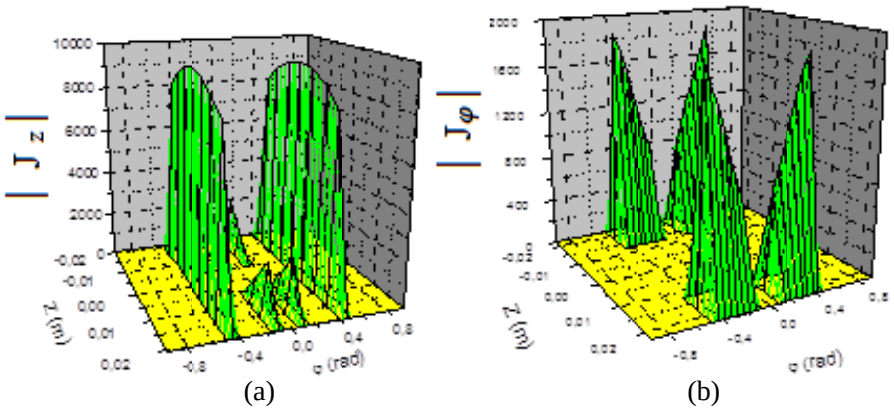

Figure 3. Amplitude distributions of the (a) z- and (b) φ- components of the surface current density on the pair of coupled slotted strip-frame patches.

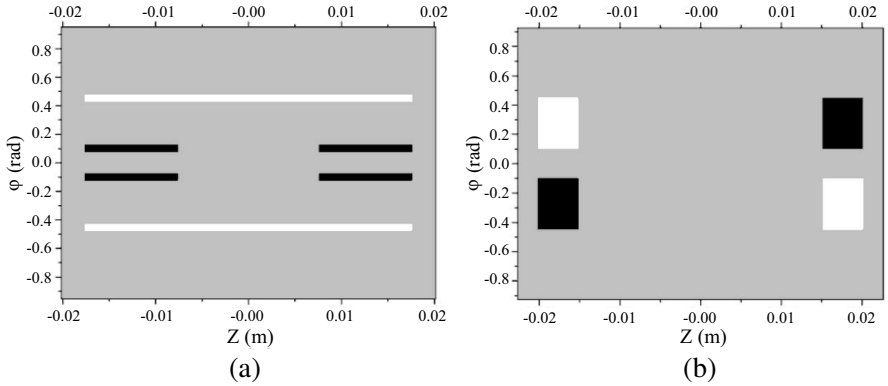

Figure 4. Phase distributions of the (a) z- and (b) φ-components of the surface current density on the pair of coupled slotted strip-frame patches.

The amplitude distribution of the φ-component current density is symmetric with respect to the plane $\varphi = 0°$. But the phase distribution is asymmetric.

2.4. Analysis of the Behavior of S_{11} for the Pair of Strip-frame Patches When a Planar Structure Is Fed by a Microstrip Line

In order to test the results of the pair of coupled strip-frame patches, a comparison to the planar case is performed. Consider the situation where the pair of coupled slotted strip-frame patches from Fig. 1(c) is placed on a plane dielectric substrate backed by a metal plane. The microstrip line feed of the patch is shown in Fig. 5(a). The constitutive and the geometrical parameters of the planar microstrip antenna and the above-considered cylindrical antenna are the same, with the geometrical dimension $W_{str} = L_u = 0.129\,\text{cm}$ added. The planar microstrip array calculations were performed with the simulation package Sonnet 12.53. The resulting reflection versus frequency is plotted in Fig. 5(b). At resonant frequency $f = 1.2737\,\text{GHz}$, the reflection coefficient $|S_{11}| = -6.48\,\text{dB}$ is at its minimum.

The resonant frequencies of the pair of coupled slotted strip-frame patches in the cylindrical (Fig. 2, curve 2) and planar (Fig. 5(b)) cases agree very well. The difference is within 0.12%.

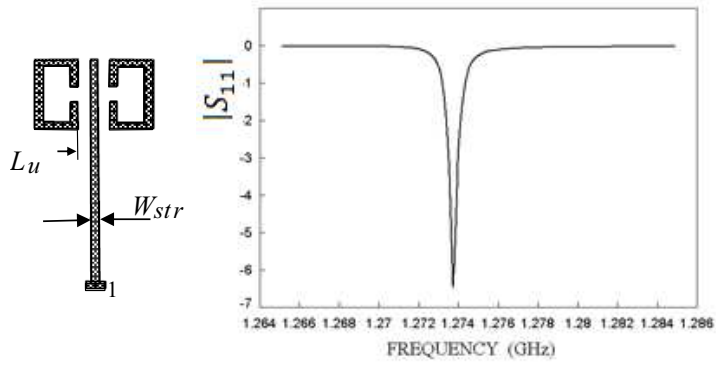

Figure 5. (a) Planar microstrip antenna with a pair of coupled slotted strip-frame patches fed by a microstrip line, (b) reflection coefficient versus frequency.

3. CYLINDRICAL MICROSTRIP ARRAY ANTENNA WITH SLOTTED STRIP-FRAMED PATCHES

3.1. Problem Formulation and Solution by the Moment Method in the Spectral Domain

Consider the cylindrical microstrip antenna array (CMAA) shown in Fig. 6, consisting of 10 patches, each like a slotted strip frame. The structure is symmetrical about the CML, $\varphi = 0°$. The patches lie on each side of the CML so that the slot faces the CML and the opposite patch slot. For geometrical details of the single and coupled patches, see Figs. 1(b) and 1(c). The CML begins at $z = z_{oc}$ (the lower open end) and ends at $z = z_f$ (the upper open end). The delta-generator location is $z = z_g$.

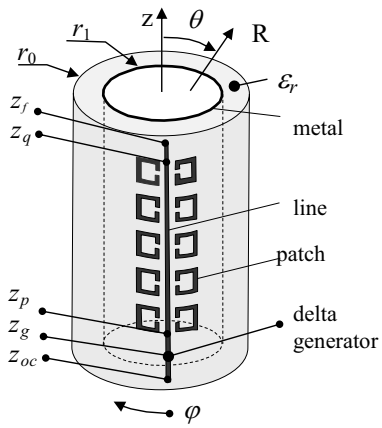

Figure 6. The radiating structure — the CMAA of 10 patches.

In our theoretical model, the CML and the patch array are thought of as a single patch of complex geometry. In this case, applying the moment method to the integral equation for the patch current density yields a SLAE (12), where the elements of its right-hand side column $\mathbf{V}$ [44] are

$$V_i = \begin{cases} -1V, & z = z_g \\ 0, & \text{otherwise} \end{cases} \tag{32}$$

The solution of (12) with right-hand side (32) yields the current density distributions on the patches and along the microstrip line. Then, as for the planar microstrip antenna, the reflection coefficient in the CML and the value of the CMAA input impedance can be evaluated using the equivalent scheme method [44] by virtue of the fact that

the CML supports a single quasi-TEM wave. This is true when the CML is electrically small (the metal cylinder radius is smaller than the wavelength, $r_1 < \lambda$, where λ is the free-space wavelength) and the dielectric substrate is thin enough ($r_0 - r_1 = d \ll \lambda$), which is the case for the problem under consideration.

To find the reflection coefficient in the CML, the standing wave pattern is analyzed on the length $z_g < z < z_p$ between the delta-generator and the point z_p, where the first patch begins. In this case, to minimize reflections from the CML open end ($z = z_{oc}$), the delta-generator should be at a quarter wavelength from the CML right open end ($z_g - z_{oc} \approx \lambda_g/4$, where λ_g is the quasi-TEM CML wavelength). Alternatively, the space $\Delta z = z_p - z_g$ should not be smaller than $\lambda_g/2$ in order to allow the standing wave simulation.

3.2. Results & Discussion

The analyzed structure (Fig. 6) has a metal cylinder of radius $r_1 = 2.5\,\text{cm}$. The dielectric substrate thickness is $d = 0.762\,\text{mm}$, the relative permittivity is $\varepsilon_r = 2.2$. The array consists of 10 strip-frame patches, $W_z = 3.664\,\text{cm}$, $W_\varphi = 1.832\,\text{cm}$, $L_\varphi = L_z = 0.458\,\text{cm}$, and $L_a = 0.916\,\text{cm}$ each, for each patch, with the center-to center distance being 17.404 cm. The patch slot is symmetrically located. The array is $z_q - z_p = 73.28\,\text{cm}$ long in the z-direction. Each patch is $L_u = L_\varphi/2$ apart from the CML. The CML width is $W_{str} = 0.229\,\text{cm}$, the length is $z_f - z_{oc} = 100.302\,\text{cm}$. The lower open end of the CML is $z_p - z_{oc} = 26.564\,\text{cm}$ away from the first patch of the array and sticks out of the array by $z_f - z_q = 0.458\,\text{cm}$. Each patch is split into 8×8 segments of size $L_z \times L_\varphi/2$. The CML structure and the patch array are meshed similarly.

In Fig. 7, the cylindrical and the planar structures of equal linear dimensions are compared for their frequency dependences of the reflection coefficients in the CML. Curve 1 (circles) describes the cylindrical CMAA and comes from the standing wave analysis on the length $z_g < z < z_p$. The resonant frequency is $f = 1.35\,\text{GHz}$, with the minimum reflection coefficient $|S_{11}| = -8.48\,\text{dB}$. Curve 2 (triangles) is for the planar microstrip array simulated with Sonnet 12.53. The resonant frequency difference between the cylindrical and the planar arrays is within 0.4%.

Figures 8(a), (b) come from the solution of the SLAE (15) and presents the amplitude (Fig. 8(a)) and the phase (Fig. 8(b)) of the surface current z-component on the patches and on the CML at resonant frequency $f = 1.35\,\text{GHz}$. Notice that the amplitude and the phase of the z- and φ-components of the electric current of a single patch in the array behave as in Figs. 3 and 4. For the array

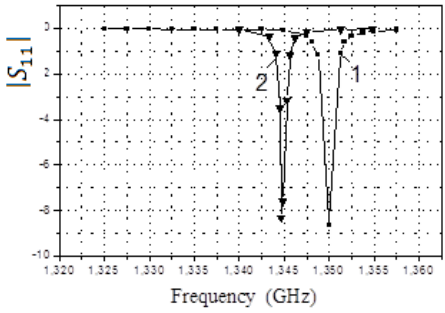

Figure 7. The reflection coefficient versus frequency: 1 — CMAA and 2 — planar microstrip array antenna.

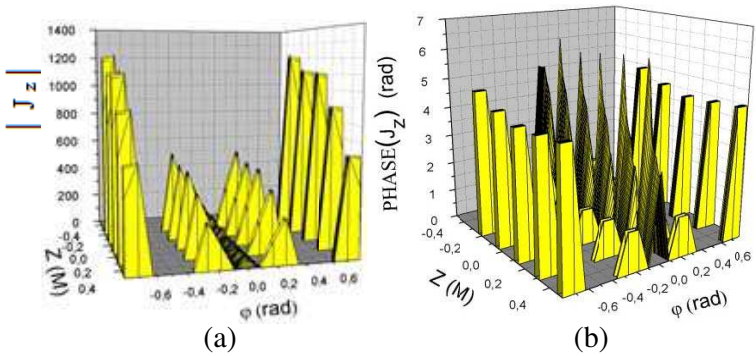

Figure 8. The current z-component (a) amplitude and (b) phase distributions on CMAA patches and CML at resonant frequency $f = 1.35\,\text{GHz}$.

as a whole it is observed that there is a relative decay of the z-current amplitude in the array from patch to patch (see Fig. 8(a)) while the phase (see Fig. 8(b)) remains constant. Also it is seen from Fig. 8(a) that for any coupled pairs of patches the z-component of the patch current density on the outer side sometimes prevails over the current density on the slotted side of the patch and they both are considerably larger than the CML current density. The identical planar antenna array was examined at resonant frequency $f = 1.3448\,\text{GHz}$ by using the simulation package Sonnet 12.53. The current distribution resembles the CMAA current distribution (see Fig. 8). Comparing the slotted strip-frame patch and the custom, similarly sized rectangular cylindrical patch, $W_z = 3.664\,\text{cm}$, $W_\varphi = 1.832\,\text{cm}$ shows that the former has far more pronounced resonant properties (see the bandwidth in Fig. 2). Its resonant frequency ($f = 1.35\,\text{GHz}$) is substantially lower than the resonant frequency ($f = 2.75\,\text{GHz}$) of

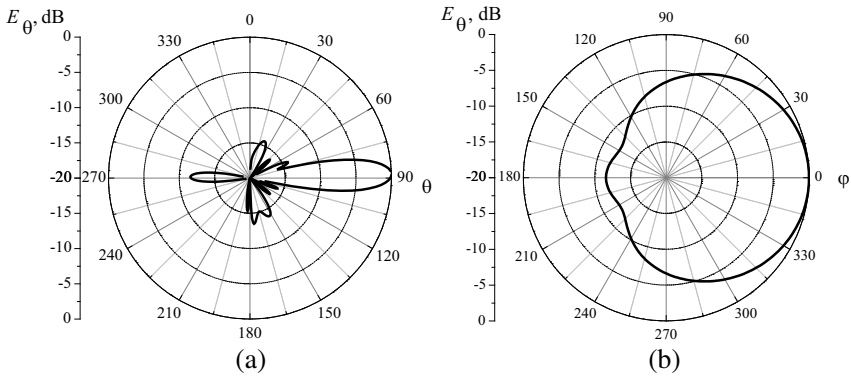

Figure 9. The CMAA radiation patterns at resonant frequency $f = 1.35\,\text{GHz}$: the E_θ-component versus θ with (a) $\varphi = 0°$ and versus φ with (b) $\theta = 90°$.

the rectangular cylindrical patch.

Figures 9(a) and (b) plot the far-field radiation patterns of the E_θ-component versus θ at $\varphi = 0°$ (a) and versus φ at $\theta = 90°$ (b). The CMAA pattern shows a sole main lobe at $\theta = 88°$. The sidelobe level does not exceed $-14\,\text{dB}$ within $0° < \theta < 180°$ in the forward radiation case.

A spatial radiation pattern analysis reveals that the back lobe, $\theta = 272°$ (Fig. 9(a) is actually the main lobe for $\varphi = 180°$ (Fig. 9(b)). This takes place when the spatial radiation pattern tends to be conical with $\theta = 88° = \text{const}$. In this case, the forward to backward radiation ratio is 11.5 dB. The cross polarization of the antenna is lower than $-40\,\text{dB}$. This low amount of cross polarization is provided by the specific phase distribution of the current density on the pair of coupled slotted strip-frame patches in the symmetrical excitation case. Namely, the contribution of the current φ-component to the radiation pattern is minimum (see Figs. 4(b) and 5(b)).

The Q factor of the main resonance is $Q \approx 700$. This is good enough for many narrow-band antennas and multifrequency antennas. In the millimeter wave region, the single-patch bandwidth can be extended by increasing the substrate thickness to $\lambda/(4\sqrt{\varepsilon_r})$.

The current distributions on the patch and along the feed line were thoroughly analyzed. A mixed regime is observed, in the sense that both standing-wave and traveling-wave regimes hold simultaneously in the CML at the patch array location. For the discussed configuration the standing-wave regime prevails over the travelling-wave regime. As the number of patches increases, the traveling-wave regime will become dominating.

4. CONCLUSION

Cylindrical microstrip structures with slotted strip-frame patches, single and coupled, have been examined for the first time. It has been shown that both patch varieties have substantially lower resonant frequencies than analogous rectangular cylindrical patches. Resonant frequencies of a pair of coupled slotted strip-frame patches in the planar and cylindrical cases agree very well (within 0.12%). This is explained by the common nature of the low frequency slot resonance, which takes place in both cases.

A cylindrical microstrip antenna array with 5 pairs of coupled slotted strip-frame patches proximity-fed by a microstrip line of about 5 wavelengths in size has been proposed. Rigorous analysis of such large proximity-fed cylindrical arrays has not been realised before. The time consumed has been reduced considerably by using a special technique in which asymptotes of the spectral Green's functions have been extracted.

An extremely low level of cross polarization ($< -40\,\mathrm{dB}$) was obtained. A very good agreement (0.4%) for resonant frequencies and resonant current distributions is observed between the cylindrical and planar antenna versions. The fact that these two arrays were analyzed by two different methods provides an extra validation of the model used for the cylindrical microstrip antenna.

Slotted strip-frame patches are promising, also at mm wave frequencies, because there are no direct electrical contacts in the microstrip line feed case. The advantage of the proximity fed antenna array consists of the fact that the effective patch-to-CML coupling is controlled by varying the space between the CML and the patches. The slot size and the patch shape do not need to be changed. Therefore the weak coupling regime may allow providing different classical array profiles of the current distributions on the elements like cosine, cosine-quadratic, etc.. It also allows antennas with a series feed of several tens of wavelengths.

The proposed theoretical model can be effectively used for the analysis of patch arrays with other complex shapes.

ACKNOWLEDGMENT

This work has been performed in the framework of the project CONFORMAL supported by the FP7 Marie Curie IIF grant 298204.

REFERENCES

1. Wang, X., M. Zhang, and S.-J. Wang, "Practicability analysis and application of PBG structures on cylindrical conformal microstrip antenna and array," *Progress In Electromagnetics Research*, Vol. 115, 495–507, 2011.
2. Li, R., L. Xu, X. W. Shi, L. Chen, and C. Y. Cui, "Two-dimensional NC-music DOA estimation algorithm with a conformal cylindrical antenna array," *Journal of Electromagnetic Waves and Applications*, Vol. 25, Nos. 5–6, 805–818, 2011.
3. Yang, P., F. Yang, and Z.-P. Nie, "DOA estimation with sub-array divided technique and interpolated esprit algorithm on a cylindrical conformal array antenna," *Progress In Electromagnetics Research*, Vol. 103, 201–216, 2010.
4. Wang, Y., Y.-J. Xie, and H. Feng, "Analysis of cylindrically conformal microstrip structures using an iterative method," *Progress In Electromagnetics Research*, Vol. 87, 215–231, 2008.
5. Cooray, F. R. and J. S. Kot, "Analysis of radiation from a cylindrical-rectangular microstrip patch antenna loaded with a superstrate and an air gap, using the electric surface current mode," *Progress In Electromagnetics Research*, Vol. 67, 135–152, 2007.
6. Li, L. W., T. X. Zhao, M. S. Leong, and T. S. Yeo, "A spatial domain method of moments analysis of a cylindrical-rectangular chirostrip," *Progress In Electromagnetics Research*, Vol. 35, 165–182, 2002.
7. Bertuch, T., F. Vipiana, and G. Vecchi, "Efficient analysis of printed structures of arbitrary shape on coated cylinders," *IEEE Trans. on Antennas and Propagation*, Vol. 60, No. 3, 1425–1439, 2012.
8. Wu, K. Y. and J. F. Kaufman, "Radiation pattern computation for cylindrical-rectangular microstrip antenna," *Antennas and Propagation Society International Symposium*, Vol. 21, 39–42, 1983.
9. Luk, K. M., K. F. Lee and J. S. Dahele, "Analysis of the cylindrical-rectangular patch antenna," *IEEE Trans. on Antennas and Propagation*, Vol. 37, No. 2, 143–147, 1989.
10. Habashy, T. M., S. M. Ali, and J. A. Kong, "Input impedance and radiation pattern of cylindrical-rectangular and wraparound microstrip antennas," *IEEE Trans. on Antennas and Propagation*, Vol. 38, No. 6, 722–731, 1990.
11. Silva, F. C., S. B. A. Fonseca, A. J. M. Soares, and A. J. Giarola,

"Analysis of microstrip antennas on circular-cylindrical substrates with a dielectric overlay," *IEEE Trans. on Antennas and Propagation*, Vol. 39, No. 9, 1398–1404, 1991.

12. Vecchi, G., T. Bertuch, and M. Orefice, "Analysis of cylindrical printed antennas with subsectional basis functions in the spectral domain," *Proceedings of the International Conference on Electromagnetics in Advanced Applications (ICEAA96)*, 301–304, Torino, Italy, 1996.
13. Bertuch, T., G. Vecchi, and M. Orefice, "Efficient spectral-domain simulation of conformal antennas of arbitrary shapes printed on circular cylinders," *Proceedings of the Millennium Conference on Antennas & Propagation*, Davos, Switzerland, April 9–14, 2000 (CD ROM).
14. Erturk, V. B. and R. G. Rojas, "Efficient analysis of input impedance and mutual coupling of microstrip antennas mounted on large coated cylinder," *IEEE Trans. on Antennas and Propagation*, Vol. 51, No. 4, 739–748, 2003.
15. Raffaelli, S., Z. Sipus, and P. S. Kildal, "Analysis and measurements of conformal patch array antennas on multilayer circular cylinder," *IEEE Trans. on Antennas and Propagation*, Vol. 53, No. 3, 1105–1113, 2005.
16. Svezhentsev, A. Y. and G. A. E. Vandenbosch, "Efficient spatial domain moment method solution of cylindrically rectangular microstrip antennas," *IEE Proceedings, Microwaves, Antennas and Propagation*, Vol. 153, No. 4, 376–384, August 2006.
17. Svezhentsev, A. Y., "Input impedance of a cylindrical microstrip antenna with patches of an arbitrary shape fed by a microstrip line," *Proceedings of 5rd European Workshop on Conformal Antennas*, 80-83, Bristol, United Kingdom, September 10–11, 2007.
18. Svezhentsev, A. Y., "Input impedance of a probe-fed cylindrical microstrip antenna. Effective calculation of probe excitation field," *Proceedings of 3rd European Conference on Antennas and Propagation (Eucap)*, 2477–2480, Berlin, Germany, March 23–29 2009.
19. Svezhentsev, A. Y. and V. V. Kryzhanovskiy, "Patch shape influence upon radar cross section of a cylindrical microstrip antenna," *Progress In Electromagnetic Research B*, Vol. 5, 307–324, 2009.
20. Bhartia, P., K. V. S. Rao, and R. S. Tomar, *Millimeter-wave Microstrip and Printed Circuit Antennas*, Artech House, Inc., Boston, London, 1991.

21. Owens, R. P., "The design and manufacture of serpent arrays and parasitic patch arrays," *IEE Colloq. 1982/19, Advances in Printed Antenna Design and Manufacture*, 4.1–4.3, February 1982.
22. Pozar, D. M. and S. M. Voda, "A rigorous analysis of a microstripline fed patch," *IEEE Trans. on Antennas and Propagation*, Vol. 35, No. 12, 1343–1350, 1987.
23. Asimakis, N. P., I. S. Karanasiou, and N. K. Uzunoglu, "Non-invasive microwave radiometric system for intracranial applications: A study using the conformal L-notch microstrip patch antenna," *Progress In Electromagnetics Research*, Vol. 117, 83–101, 2011.
24. Wang, X., M. Zhang, and S.-J. Wang, "Practicability analysis and application of PBG structures on cylindrical conformal microstrip antenna and array," *Progress In Electromagnetics Research*, Vol. 115, 495–507, 2011.
25. Liang, J. and D. Liu, "Two L-shaped array-based 2-D DOAs estimation in the presence of mutual coupling," *Progress In Electromagnetics Research*, Vol. 112, 273–298, 2011.
26. Zhu, X., W. Shao, J.-L. Li, and Y.-L. Dong, "Design and optimization of low RCS patch antennas based on a genetic algorithm," *Progress In Electromagnetics Research*, Vol. 122, 327–339, 2012.
27. Weng, W.-C. and C.-L. Hung, "Design and optimization of a logo-type antenna for multiband applications," *Progress In Electromagnetics Research*, Vol. 123, 159–174, 2012.
28. Exposito-Dominguez, G., J.-M. Fernandez Gonzalez, P. Padilla de la Torre, and M. Sierra-Castaner, "Dual circular polarized steering antenna for satellite communications in X band," *Progress In Electromagnetics Research*, Vol. 122, 61–76, 2012.
29. Xie, J.-J., Y.-Z. Yin, J. Ren, and T. Wang, "A wideband dual-polarized patch antenna with electric probe and magnetic loop feeds," *Progress In Electromagnetics Research*, Vol. 132, 499–515, 2012.
30. Ahdi Rezaeieh, S. and M. Kartal, "A new triple band circularly polarized square slot antenna design with crooked T and F-shape strips for wireless applications," *Progress In Electromagnetics Research*, Vol. 121, 1–18, 2011.
31. Gujral, M., J. L.-W. Li, T. Yuan, and C.-W. Qiu, "Bandwidth improvement of microstrip antenna array using dummy EBG pattern on feedline," *Progress In Electromagnetics Research*, Vol. 127, 79–92, 2012.

32. Wei, K., Z. Zhang, and Z. Feng, "Design of a dualband omnidirectional planar microstrip antenna array," *Progress In Electromagnetics Research*, Vol. 126, 101–120, 2012.
33. Sze, J.-Y. and S.-P. Pan, "Design of broadband circularly polarized square slot antenna with a compact size," *Progress In Electromagnetics Research*, Vol. 120, 513–533, 2011.
34. Peng, H.-L., W.-Y. Yin, J.-F. Mao, D. Huo, X. Hang, and L. Zhou, "A compact dual-polarized broadband antenna with hybrid beam-forming capabilities," *Progress In Electromagnetic Research*, Vol. 118, 253–271, 2011.
35. Moradi, K. and S. Nikmehr, "A dual-band dual-polarized microstrip array antenna for base stations," *Progress In Electromagnetic Research*, Vol. 123, 527–541, 2012.
36. Wang, P., G. Wen, J. Li, Y. Huang, L. Yang, and Q. Zhang, "Wideband circularly polarized UHF RFID reader antenna with high gain and wide axial ratio beamwidths," *Progress In Electromagnetics Research*, Vol. 129, 365–385, 2012.
37. Panda, J. R. and R. S. Kshetrimayum, "A printed 2.4 GHz/5.8 GHz dual-band monopole antenna with a protruding stub in the ground plane for WLAN and RFID applications," *Progress In Electromagnetics Research*, Vol. 117, 425–434, 2011.
38. Goubau, G., "Surface waves and their applications transmission lines," *J. Appl. Phys.*, Vol. 21, No. 11, 1119–1128, 1950.
39. Stratton, J. A., *Electromagnetic Theory*, New York and London, 1941.
40. Schelkunoff, S. A., "Some equivalence theorems of electromagnetics and their application to radiation problems," *Bell Syst. Tech. Journ.*, Vol. 15, 92, 1936.
41. Abramowitz, M. and I. A. Stegun, *Handbook of Mathematical Functions*, Dover, New York, 1971.
42. Svezhentsev, A. Y. and G. A. E. Vandenbosch, "Mixed-potential Green's functions for sheet electric current over metal-dielectric cylindrical structure," *Journal of Electromagnetic Waves and Application*, No. 6, 813–835, 2002.
43. Svezhentsev, A. Y. and G. A. E. Vandenbosch, "Spatial Green's function singularity for sheet electric current over dielectric coated cylinder," *IEEE Trans. on Antennas and Propagation*, Vol. 52, No. 2, 608–611, 2004.
44. Davidovitz, M. and Y. T. Lo, "Rigorous analysis of a circular patch antenna excited by a microstrip line," *IEEE Trans. on Antennas and Propagation*, Vol. 37, No. 8, 949–958, 1989.